

# Daily to centennial behavior of aseismic slip along the central section of the North Anatolian Fault

R. Jolivet<sup>1,2</sup>, J. Jara<sup>1</sup>, M. Dalaison<sup>1</sup>, B. Rouet-Leduc<sup>3</sup>, A. Özdemir<sup>4</sup>, U.  
Dogan<sup>4</sup>, Z. Çakir<sup>5</sup>, S. Ergintav<sup>6</sup>

<sup>1</sup>Laboratoire de Géologie, Département de Géosciences, École Normale Supérieure, PSL Université, CNRS  
UMR 8538, Paris, France

<sup>2</sup>Institut Universitaire de France, 1 rue Descartes, 75006 Paris

<sup>3</sup>Disaster Prevention Research Institute, Kyoto University, Kyoto, Japan

<sup>4</sup>Department of Geomatic Engineering, Yildiz Technical University, 34220 Istanbul, Turkey

<sup>5</sup>Department of Geology, Istanbul Technical University, 34469 Istanbul, Turkey

<sup>6</sup>Department of Geodesy, Kandilli Observatory and Earthquake Research Institute, Bogazici University,  
34684 Istanbul, Turkey

## Key Points:

- We image the spatio-temporal variations of aseismic slip along the central section of the North Anatolian Fault with InSAR and GNSS data
- Slow slip extends over 70 km, reaches 1 cm/yr and coincides with shallow locking depth along the fault
- Slow slip events do not occur along the whole creeping section but have been detected since, at least, the 1980's

---

Corresponding author: Romain Jolivet, [romain.jolivet@ens.fr](mailto:romain.jolivet@ens.fr)

20 **Abstract**

21 Slow, aseismic slip plays a crucial role in the initiation, propagation and arrest of large  
22 earthquakes along active faults. In addition, aseismic slip controls the budget of elas-  
23 tic strain in the crust, hence the amount of energy available for upcoming earthquakes.  
24 The conditions for slow slip include specific material properties of the fault zone, pore  
25 fluid pressure and geometrical complexities of the fault plane. Fine scale descriptions of  
26 aseismic slip at the surface and at depth are key to determine the factors controlling the  
27 occurrence of slow, aseismic versus rapid, seismic fault slip. We focus on the spatial and  
28 temporal distribution of aseismic slip along the North Anatolian Fault, the plate bound-  
29 ary accommodating the 2 cm/yr of relative motion between Anatolia and Eurasia. Along  
30 the eastern termination of the rupture trace of the 1944 M7.3 Bolu-Gerede earthquake  
31 lies a segment that slips aseismically since at least the 1950's. We use Sentinel 1 time  
32 series of displacement and GNSS data to provide a spatio-temporal description of the  
33 kinematics of fault slip. We show that aseismic slip observed at the surface is coincident  
34 with a shallow locking depth and that slow slip events with a return period of 2.5 years  
35 are restricted to a specific section of the fault. In the light of historical measurements,  
36 we discuss potential rheological implications of our results and propose a simple alter-  
37 native model to explain the local occurrence of shallow aseismic slip at this location.

38 **Plain Language Summary**

39 Earthquakes are the manifestation of the rapid release of elastic energy stored in  
40 the crust under the action of moving tectonic plates along a plate boundary fault sys-  
41 tem. Interestingly, some faults exhibit a slow and harmless release of energy under the  
42 form of aseismic slip. The conditions for slow slip, opposed to earthquakes, are not fully  
43 understood and it appears of higher importance to study high-resolution, small scale fea-  
44 tures to grow our understanding. We analyze satellite Radar imagery and GNSS data  
45 to build a movie of ground motion in the vicinity of the North Anatolian Fault in Turkey  
46 over a section that was recognized to slip aseismically in the 70's. We show that aseis-  
47 mic slip there is made of slow slip events repeating every 2.5 years embedded within a  
48 larger region that slips steadily at least since 2007. Using these data, we model the dis-  
49 tribution of slip rates at depth on the fault and show that aseismic slip extends at depth  
50 until 5-8 km. Below, the fault is locked, accumulating energy for upcoming earthquakes.  
51 In the light of past measurements and based on our high-resolution dataset, we discuss  
52 potential physical models explaining the occurrence of slow slip in this region.

## 1 Introduction

The discovery of slow, aseismic slip in the 1960's both along the San Andreas Fault (Steinbrugge et al., 1960) and the North Anatolian Fault (Ambraseys, 1970) led to a revision of the elastic rebound theory proposed by Reid (1911). Slow slip has now been described along numerous active faults, including the San Andreas Fault (e.g. Steinbrugge et al., 1960; Jolivet, Simons, et al., 2015), the North Anatolian Fault (e.g. Ambraseys, 1970; Çakir et al., 2005), the Leyte fault (e.g. Duquesnoy et al., 1994; Dianala et al., 2020) among others (see a more exhaustive description in Jolivet and Frank (2020)), and is now recognized as one end-member mode of fault slip releasing stress along active faults. Slow slip has also been described along subduction megathrust either in the form of transient events (e.g. Dragert et al., 2001; Wallace, 2020), associated with tremors or not, and as variations of megathrust kinematic coupling (e.g. Mazzotti et al., 2000; Avouac, 2015). Observationally, slow slip has been linked with the preparation phase of earthquakes, such as before the  $M_w$ 8.1 Iquique earthquake in Chile in 2014 (e.g. Ruiz et al., 2014; Socquet et al., 2017) or, more disputably, before the  $M_w$ 7.4 Izmit earthquake in 1999 in Turkey (Bouchon et al., 2011; Ellsworth & Bulut, 2018). Effectively, slow slip, like earthquakes, contributes to the release of elastic energy that accumulates under the loading imposed by tectonic motion (e.g. Avouac, 2015). As a result, slow slip influences the size of large earthquakes which are known to be arrested preferentially by fault segments hosting aseismic slip (e.g. Kaneko et al., 2010), among other causes.

Although the importance of aseismic slip on the dynamics of earthquakes is indisputable (e.g. Avouac, 2015; Bürgmann, 2018), the physical mechanisms responsible for keeping slip slow are still unclear. Multiple mechanisms may be involved to prevent fault slip to become dynamic and reach slip speeds characteristic of earthquakes ( $\sim 1$  m/s). First, the spatial distribution of rheological properties of the fault material governs the spatial and temporal evolution of fault slip. For instance, rate strengthening fault material leads to stable slip (e.g. Scholz, 1998; Thomas et al., 2017). As fault rheology, and in particular the constitutive properties of the law controlling friction on the fault plane, depend on temperature and normal stress, the resulting depth-dependent distribution of fault properties explains the depth distribution of slip modes in a variety of subduction zones and continental faults (e.g. Blanpied et al., 1991; den Hartog & Spiers, 2013). Second, if fault frictional properties lead to a rate weakening behavior, a large nucleation size (i.e. the slip distance over which slip becomes dynamic) may prevent slip to reach

86 seismic speeds (e.g. Ampuero & Rubin, 2008). As nucleation size depends on both con-  
87 stitutive properties and effective normal stress, one may invoke the influence of elevated  
88 pore fluid pressure to keep slip stable, as observed at the deep end of the potentially seis-  
89 mogenic portion of subduction megathrust (e.g. Kodaira et al., 2004; Moreno et al., 2014).  
90 Third, recent works suggest that complexities in the fault geometry may lead to the emer-  
91 gence of slow slip even with unstable rate-weakening properties, either through local mod-  
92 ulation of normal stress due to slip on a rough fault (Cattania & Segall, 2021) or to stress  
93 interactions between fault segments (Romanet et al., 2018). In all cases, it is important  
94 to realize that the geological conditions underlying these physical mechanisms may vary  
95 over a wide range of length scales. Rock types, pore fluid pressure and fault geometry  
96 may vary over any distances, from millimeters to hundreds of kilometers. Fault geom-  
97 etry for instance is considered self-similar and has no characteristic length scale (e.g. Can-  
98 dela et al., 2012).

99 It is therefore of uttermost importance to provide descriptions of aseismic, slow slip  
100 with the highest level of details over large regions. In subduction zones, the vast major-  
101 ity of geodetic and seismological stations are necessarily located on land, far from the  
102 megathrust. To the contrary, the surface expression of continental faults can be stud-  
103 ied with high levels of detail due to available Interferometric Synthetic aperture radar  
104 (InSAR) data, near-field GNSS stations and creepmeters, which may reveal the small-  
105 est details of aseismic slip. For instance, Jolivet, Candela, et al. (2015) and Khoshmanesh  
106 and Shirzaei (2018) have explored the occurrence of clusters of slow slip events with scales  
107 from tens of meters to tens of kilometers, suggesting an avalanche-like behavior witness-  
108 ing interactions between slow slip events. Dalaison et al. (2021) show the complex pat-  
109 tern of slow and rapid slip along the Chaman fault in Pakistan which hosts one of the  
110 longest creeping sections on Earth. In this paper, we explore and describe the behav-  
111 ior of aseismic slip along the Isetmpasa section of the North Anatolian Fault, covering  
112 time scales ranging from days to decades and length scales from hundreds of meters to  
113 tens of kilometers.

## 114 **2 Seismo-tectonic setting and motivation**

115 First mentions of aseismic slip along the North Anatolian Fault date from Ambraseys  
116 (1970). In particular, Ambraseys (1970) describes the offset of a wall in the city of Is-  
117 metpasa which was not related to any significant seismic activity. Although the paper

118 mentions that it is not known whether the offset occurred gradually or episodically, a  
119 first creep rate of 2 cm/yr was inferred while the earlier offset of railroad tracks in the  
120 same place suggested a 5 cm/yr creep rate from 1944 to 1950. Following the suggestion  
121 of Ambraseys (1970), Bilham et al. (2016) re-evaluated these surface slip rates, inferring  
122 slightly slower rates. The 1944 M 7.4 Gerede earthquake is the last large event known  
123 to have ruptured in this area, and those early estimates fall within the subsequent post-  
124 seismic period (e.g. Fig. 1 and Kondo et al., 2010). Since then, numerous studies have  
125 measured surface slip rates, using land-based and geodetic techniques, including creep-  
126 meters, GNSS data and InSAR data (Aytun, 1982; Eren, 1984; Deniz et al., 1993; Al-  
127 tay & Sav, 1991; Çakir et al., 2005; Kutoglu & Akcin, 2006; Kutoglu et al., 2008, 2010;  
128 Karabacak et al., 2011; Deguchi, 2011; Kaneko et al., 2012; Ozener et al., 2013; Cetin  
129 et al., 2014; Bilham et al., 2016). All subsequent studies infer a surface creep rate, at Is-  
130 metpasa, of about 6 to 8 mm/yr, since at least the 1980's. The decrease in slip rate from  
131 5 cm/yr followed by a rather constant rate of 6 to 8 mm/yr was interpreted as the sig-  
132 nature of a long lived post-seismic signal and modeled with rate-and-state friction (Kaneko  
133 et al., 2012). The model suggests that shallow material, from the surface to a depth of  
134 about 5 km, is rate strengthening, promoting shallow afterslip. Prompting adequate tun-  
135 ing of the constitutive parameters of the friction law, this model can produce long lived  
136 afterslip lasting more than 55 years. It is important to realize that all these measure-  
137 ments were made and restricted to a single location along the fault and that the slip rates  
138 measured following the 1944 earthquake are uncertain (Bilham et al., 2016).

139 Slow slip events were recently discovered at Ismetpasa (Bilham et al., 2016; Rous-  
140 set et al., 2016). In 2013, a 2 cm slow slip event was detected from time series analysis  
141 of InSAR data acquired by the Cosmo-Skymed constellation (Rousset et al., 2016). Slip  
142 spanned a 10 km-long section of the fault with a 4 km width along dip. Such event echoes  
143 the surface slip accelerations inferred from creepmeter records in the 1980's (Altay & Sav,  
144 1991) and those currently captured by the creepmeter operating since 2014 (Bilham et  
145 al., 2016). The largest slow slip events are spontaneous as they do not follow significant  
146 earthquakes or identified stress perturbation. They repeat every 2 to 3 years with slip  
147 amplitudes that vary from 5 to 15 mm. If such events occur, then the rheology of the  
148 fault cannot be simply rate-strengthening and two possibilities arise. Rheology is either  
149 rate-weakening, hence promoting spontaneous slip instabilities although such instabil-

ities cannot become dynamic, either it is heterogeneous with unstable fault patches embedded in a generally stable matrix (Wei et al., 2013).

In all cases, several questions are left unanswered considering the slip rate variations and distribution along the creeping section of Ismetpasa. First, although the spatial distribution of slip has already been inferred (Cetin et al., 2014), it is unclear how deep slip extends and what are the uncertainties associated with the slip distribution. Large scale strain mapping and modeling are not sufficient and fine exploration of the deformation field in this area is required (Weiss et al., 2020; Barbot & Weiss, 2021). Second, temporal variations of slip rate have, so far, only been detected at Ismetpasa. Is such episodic behavior representative of the whole fault section or not?

To address these questions, we derive time series of surface displacements over the 2014-2021 period from Sentinel 1 InSAR data and explore the spatial and temporal behavior of aseismic slip along this creeping section. We also include ground velocity measured at GNSS sites from the National Turkish network and preliminary results from a network of near-fault GNSS sites designed at capturing slow slip events. In the following, after specifying our approach, we describe the resulting surface velocity field and infer the distribution of average slip rates at depth along with associated uncertainties. We then explore potential surface slip rate variations to detect small slow slip events over the whole extent of the creeping section. We finally discuss the occurrences of such slow events in the light of previously measured surface slip rates and elaborate on the rheology of the fault zone.

### 3 Data processing

#### 3.1 InSAR data processing

We process all available Synthetic Aperture Radar data from the Sentinel 1 constellation from 2014 to late 2020 with the ISCE processing environment (JPL/Caltech, [winsar.unavco.org/isce.html](http://winsar.unavco.org/isce.html); Gurrola et al., 2010) using the same approach as Dalaison et al. (2021). We process data from descending tracks 65 and 167 and ascending track 87. First, we coregister all images to a single reference acquisition chosen in the middle of the time series of images. Coregistration is performed using satellite orbits and refined using the spectral diversity available on Radar burst overlaps (Fattahi et al., 2016). From the 288, 278 and 293 acquisitions on tracks 65, 167 and 87 respectively, we then com-

181 pute 1858, 1826 and 3053 interferograms (see supplementary figures S-1 to S-3 for base-  
182 line plots). We remove the contribution of the stratified tropospheric delay from the wrapped  
183 interferograms using the ERA5 re-analysed temperature, water vapor and pressure level  
184 heights fields (Jolivet et al., 2011, 2014) using the PyAPS software (Agram et al., 2013).  
185 We look down interferograms for a final pixel size of 160 m in azimuth and range direc-  
186 tion (i.e. 8 looks in azimuth and 32 looks in range). We then filter and unwrap inter-  
187 ferograms using the adaptive phase filter and the coherence-based branch cut algorithm  
188 available in ISCE (Goldstein et al., 1988; Goldstein & Werner, 1998). We finally correct  
189 for potential unwrapping errors using the CorPhu algorithm (Benoit et al., 2020). In-  
190 dependently on each track, we use the Kalman filter approach developed by Dalaison and  
191 Jolivet (2020) to reconstruct the time series of surface displacements in the satellite Line-  
192 Of-Sight (hereafter LOS) from the set of interferograms. Since no significant earthquake  
193 has been detected in the region over the period we analyse, we only consider an annual  
194 oscillation and a secular trend as a basis model underlying the Kalman filter. We use  
195 the parameterization proposed in Dalaison and Jolivet (2020).

196 Results are shown on Fig. 1 and S-9 to S-12 of the supplementary informations.  
197 As interferograms do not unwrap completely, with especially poor coherence in the north  
198 of the area, close to the shore of the Black Sea, final reconstruction of the time series shows  
199 variable quality. We define the reconstruction Root Mean Square (RMS) as the sum of  
200 the squared difference between the interferograms and the synthetic interferograms in-  
201 ferred from our time series, divided by the total number of interferograms. We compute  
202 such RMS for each pixel of each track. We decide to mask pixels with a reconstruction  
203 RMS higher than 2 mm, pixels constrained by less than 1300 interferograms and with  
204 a final uncertainty on the velocity higher than 0.5 mm/yr. We retain for the following  
205 analysis pixels less than 60 km away from the North Anatolian Fault trace. We combine  
206 the final three LOS velocity maps into fault parallel and vertical velocity maps assum-  
207 ing horizontal motion aligns with  $77.5^\circ\text{N}$  azimuth. Final horizontal velocity is shown on  
208 figure 1 while the vertical velocity map is available on Fig. S-15 of the supplementary  
209 materials.

210 Similar to Dalaison et al. (2021), we extract fault perpendicular profiles on each  
211 LOS velocity maps every 250 m and evaluate the across fault ground velocity difference  
212 to infer the surface slip rate and the associated uncertainties (Fig. S-13 and Fig. S-14  
213 of the supplementary materials). Such slip rate is remarkably consistent between both

214 descending tracks 65 and 167 and shows opposite sign on track 87, suggesting a dom-  
215 inantly strike slip motion across the fault. We combine these along strike surface slip mea-  
216 surements into a strike slip and dip slip motion (Fig. 1 and Fig. S-14 of the supplemen-  
217 tary materials). Potential dip slip is visible between  $32.5^\circ$  and  $32.75^\circ$  W of longitude, near  
218 Ismetpasa.

### 219 3.2 GNSS data processing

220 We installed 19 permanent GNSS sites along the section previously identified as  
221 creeping by Cetin et al. (2014). Sites are located close to the fault ( $< 5$  km) in order  
222 to capture shallow slow slip events, previously captured with InSAR and creepmeter data  
223 (Altay & Sav, 1991; Bilham et al., 2016; Rousset et al., 2016). In this paper, we only seek  
224 to include velocities measured at each site of this network, hereafter referred to as Is-  
225 menet, to constrain the slip rate at shallow depths. We processed data from the Ismenet  
226 network together with 57 stations from the International GNSS service (37 sites, [www.igs](http://www.igs.org)  
227 [.org](http://www.igs.org)) and from the Turkish National Network (20 sites, [https://www.tusaga-aktif](https://www.tusaga-aktif.gov.tr/)  
228 [.gov.tr/](https://www.tusaga-aktif.gov.tr/)). A detailed description of the sites used can be found in supplementary ma-  
229 terials.

230 Observations are processed in double differences using the GAMIT/GLOBK 10.7  
231 software (Herring et al., 2018) to obtain daily estimates of station positions, choosing  
232 ionosphere-free combination and fixing the ambiguities to integer values. We use pre-  
233 cise orbits from the International GNSS Service for Geodynamics, precise EOPs from  
234 the IERS bulletin B, IGS tables to describe the phase centers of the antennas, FES2004  
235 ocean-tidal loading corrections, and atmospheric loading corrections (tidal and non-tidal).  
236 One tropospheric vertical delay parameter and two horizontal gradients per stations are  
237 estimated every 2 hours. We use the GLOBK software (Herring et al., 2018) to combine  
238 daily solutions and the PYACS software (J. Nocquet, 2018) to derive the position time  
239 series, which are then mapped into the ITRF 2014 reference frame (Altamimi et al., 2016).  
240 Finally, the time series are set in a fixed Eurasian frame, considering the pole solution  
241 proposed by Altamimi et al. (2016). We use a trajectory model to extract the velocity  
242 on each time series (Bevis & Brown, 2014) and evaluate the standard deviation on ve-  
243 locities assuming white and flicker noise following Williams (2003).

## 4 Surface velocity and average slip rate

### 4.1 Surface velocity across the North Anatolian Fault

Our velocity map is consistent with previously published results (e.g. Kaneko et al., 2012; Cetin et al., 2014). Although decoherence and poor RMS reconstruction leaves gaps in the velocity map, we clearly identify the signature of the North Anatolian Fault with a gradient of  $\sim 2$  cm/yr across the fault which varies significantly along strike (Fig. 1). Along most portions of the fault, the across fault gradient of displacement rate is gradual with a 20-30 km-wide transition from westward to eastward motion (i.e. west of  $32.4^\circ\text{N}$  and east of  $33.4^\circ\text{N}$ ).

Between  $32.4^\circ\text{N}$  and  $33.4^\circ\text{N}$ , we observe a very sharp, step-like gradient of velocity across the fault. We interpret this step-like transition as the signature of surface slip over an approximately 60 to 70 km-long profile. This surface slip rate shows a maximum slip rate of  $1 \pm 0.2$  cm/yr that tappers down to negligible values in an almost elliptical shape. Slip rate at the city of Ismetpasa (longitude  $32.63^\circ\text{N}$ ) is  $6 \pm 2$  mm/yr, consistent with published rates from creepmeter measurements (Bilham et al., 2016). Uncertainties are on the order of 2 to 3 mm/yr. The distribution of slip at the surface overlaps with both the eastern termination of the 1944 Bolu-Gerede ( $M_w 7.4$ ) earthquake and the western end of the 1943 Tosya ( $M_w 7.6$ ) earthquake (Kondo et al., 2005; Barka, 1996). This segment also overlaps with the rupture of the 1951 Kursunlu  $M_w 6.9$  earthquake, although the extent of that rupture is unclear (Ambraseys, 1970; Barka, 1996).

We observe significant vertical differential motion across the fault near the city of Ismetpasa, where the northern block subsides with respect to the southern bloc. The rate of vertical differential motion reaches locally  $12 \pm 3$  mm/yr but its extent does not exceed 15 km along strike. We also observe pronounced subsidence north of the fault, with a maximum of 10 mm/yr, over a 15 km-wide region bounded by the trace of the North Anatolian Fault to the south (Fig. 1). We account for this subsidence signal in further modeling in order not to bias slip rate estimates at depth. Other signals of vertical motion can be observed in various places in the velocity map but further away from the fault ( $> 20$  km), hence these should average out in the data decimation process and not affect our model inference. We do not observe any other subsidence signal along the fault trace. Finally, we raise the readers' attention to the fact that such subsidence is observed where previous local measurements of aseismic slip were done.

276 **4.2 Slip distribution and uncertainties**

277 The surface velocity field described above is consistent with strain localizing in the  
278 vicinity of a major strike slip, plate boundary fault. We do not observe significant sig-  
279 nals associated with other faults, hence we assume surface displacement rates originate  
280 from slip along the North Anatolian Fault at depth. Following the approach of Jolivet,  
281 Simons, et al. (2015), we consider the NAF as a vertical fault embedded in an elastic crust.  
282 Surface displacement resulting from elastic loading is usually modeled as the result of  
283 slip on an infinitely deep dislocation buried below a given locking depth (Savage & Bur-  
284 ford, 1973). Aseismic slip can be modeled as the result of shallow elastic dislocations (e.g  
285 Ryder & Bürgmann, 2008; Maurer & Johnson, 2014; Jolivet, Simons, et al., 2015; Bletery  
286 et al., 2020). Finally, local subsidence can be modeled using an *ad hoc* Mogi source with  
287 a pressure or volume change (Mogi, 1958).

288 We model the surface displacement captured by the three InSAR line-of-sight ve-  
289 locity maps and by our local GNSS network as the sum of 4 contributions. First, we solve  
290 for strike slip rate on infinitely deep dislocations following the trace of the NAF buried  
291 below 20-km-depth. This depth is chosen deep enough to reach the brittle-ductile tran-  
292 sition and to allow shallower slip on the shallow portion of the NAF in case the effec-  
293 tive locking depth is located above 20-km-depth. Second, we discretize the NAF fault  
294 plane above the locking depth up to the surface in a triangular mesh. Slip on this fault  
295 plane is the linear interpolation of slip values at each node of the triangular mesh. Tri-  
296 angle size varies from 1 km at the surface to 10 km at depth (see supp mat). Third, we  
297 model local vertical motion across the NAF at Ismetpasa by dip slip motion on a sub-  
298 set of the mesh used for strike slip. For all fault models, we compute Green’s functions  
299 relating slip to surface displacements in a semi-infinite stratified half-space using the strat-  
300 ification of elastic parameters from Rousset et al. (2016). Fourth, we include a Mogi source  
301 at an arbitrary depth of 3 km below the subsiding basin north of Ismetpasa (Mogi, 1958).  
302 We include this source to remove the potential bias on the inferred strike slip rate, we  
303 are not interested in the actual values of pressure change in the source which tradeoff  
304 with its depth and size, hence the arbitrary choice of the depth of the source.

305 In addition, we model long wavelength signals in each InSAR velocity maps (i.e.  
306 orbital errors, long wavelength atmospheric signals, etc) as a linear function of longitude  
307 and latitude. We also solve for a translation and a rotation within the GNSS velocity

308 field. Final parameter set includes slip rate on deep dislocations to model crustal elas-  
 309 tic loading, slip rate on the shallow, discretized NAF, dip slip in the vicinity of Ismet-  
 310 pasa, a Mogi source north of Ismetpasa and geometric parameters for InSAR and GNSS  
 311 common referencing.

312 We downsample the InSAR velocity maps to minimize computational burden us-  
 313 ing a quadtree approach designed to maximize resolution on the fault plane (Lohman  
 314 & Simons, 2005; Jolivet, Simons, et al., 2015). In order to avoid averaging velocities across  
 315 the fault, we exclude pixels located less than 1 km from the fault trace. Doing so, we lose  
 316 precious information on potential slip along the shallowest portion of the fault ( $< 1$  km-  
 317 depth). We therefore model the across fault step measured in the three LOS velocity maps  
 318 (Fig Sxx) and we force slip to be constant between the surface and a depth of 1 km. More-  
 319 over, to ensure continuity of slip rates at depth, we constraint slip rates along the deep-  
 320 est elements of the meshed NAF to equal those along the deep dislocations.

321 We explore the range of possible models using a Bayesian approach in order to de-  
 322 rive the posterior Probability Density Function of models. Effectively, the posterior PDF,  
 323  $\Theta(\mathbf{m}|\mathbf{d})$ , is proportional to the product of the prior PDF (i.e. our state of knowledge be-  
 324 fore considering any data),  $\rho(\mathbf{m})$ , with the likelihood (i.e. the probability that a model  
 325 will lead to a prediction that fits the data),  $L(\mathbf{d}|\mathbf{m})$ , according to Bayes' theorem, such  
 326 as

$$\Theta(\mathbf{m}|\mathbf{d}) \propto \rho(\mathbf{m})L(\mathbf{d}|\mathbf{m}), \quad (1)$$

327 where  $\mathbf{m}$  is the vector of model parameters and  $\mathbf{d}$  is the data vector. As a prior PDF,  
 328 we consider a uniform distribution from 0 to 50 mm/yr for strike slip on the shallow part  
 329 of the NAF. Since most plate reconstruction models suggest a long term slip rate of the  
 330 NAF around 20 mm/yr, we consider a uniform distribution between 10 and 30 mm/yr  
 331 for the deep dislocations (e.g. DeMets et al., 2010). We consider uniform distributions  
 332 for the parameters of the geometric transformations applied to each of the geodetic datasets.  
 333 We chose a Gaussian formulation for the likelihood such as

$$L(\mathbf{d}|\mathbf{m}) \propto \exp -\frac{1}{2}(\mathbf{G}\mathbf{m} - \mathbf{d})^T \mathbf{C}_\chi^{-1}(\mathbf{G}\mathbf{m} - \mathbf{d}), \quad (2)$$

334 where  $\mathbf{G}$  is the matrix of Green's functions. Following the approach of Duputel et al. (2014),  
 335  $\mathbf{C}_\chi$  is the sum of  $\mathbf{C}_d$ , the data covariance matrix, and  $\mathbf{C}_p$ , the matrix of prediction un-  
 336 certainties accounting for uncertainties in the elastic structure (see Rousset et al., 2016,  
 337 for a description of how we build  $\mathbf{C}_p$ ). We build the data covariance matrix assuming

338 different datasets (i.e. InSAR and GNSS velocities) are independent. We evaluate the  
339 covariance of the InSAR velocity maps over regions with no identified deformation sig-  
340 nals (e.g. Sudhaus & Jónsson, 2009; Jolivet, Simons, et al., 2015, and supp. mat.).

341 Since we use bounded uniform and Gaussian prior PDFs, there is no analytical for-  
342 mulation of the model that best fits the data, although a bounded normal distribution  
343 is expected (J. M. Nocquet, 2018). We use AlTar, a stochastic sampler using elements  
344 of parallel tempering, to draw 90,000 samples from the posterior PDF ([https://github](https://github.com/AlTarFramework/altar)  
345 [.com/AlTarFramework/altar](https://github.com/AlTarFramework/altar); Minson et al., 2013; Jolivet, Simons, et al., 2015). Do-  
346 ing so, we explore the range of models that explain the data without the use of any form  
347 of regularization (i.e. smoothing) apart from the choice of the geometry of the fault (i.e.  
348 as opposed to trans-dimensional methods, Dettmer et al., 2014). AlTar uses parallel tem-  
349 pering to let the sample set slowly converge toward the posterior PDF. Here, we need  
350 62 iterations to let the 90,000 Markov chains to converge (see supp mat for an example  
351 of convergence for the marginal of the deep slip rate on the NAF).

352 In figure 2, we show the mean of the 90,000 samples and the corresponding stan-  
353 dard deviation. First, we see that the slip rate on deep dislocations is of  $20\pm 0.6$  mm/yr.  
354 Second, we observe that the locking depth we have arbitrarily chosen is consistent with  
355 our data almost everywhere along the fault. We note that, given the large size ( $> 5$  km)  
356 of triangles of the fault mesh at the bottom end of the shallow section of the NAF, lock-  
357 ing depth can be effectively anywhere between 15 and 20 km. Below the 60-70 km long  
358 segment that slips rapidly at the surface, we observe a shallower locking depth between  
359 8 and 12 km. Along this segment, slip rates locally reach  $20\pm 3$  mm/yr with potentially  
360 two distinct patches. In addition, along this same section, we observe a locked section  
361 at depth from roughly 5 to 10 km-depth. We observe a patch of high vertical slip rate  
362 located near the city of Ismetpasa with slip rates as high as  $12\pm 3$  mm/yr, although this  
363 patch is very limited in size. Other along strike variations of slip rate are not significant  
364 compared to the standard deviation and correspond to areas where InSAR decoherence  
365 led to poor velocity reconstruction. Figures in supp. mat. show how the mean model  
366 performs at fitting the data. Note that the mean model does not belong to the ensem-  
367 ble of models drawn from the posterior PDF and is expected to show lower performance  
368 than models actually within our sample set.

As a conclusion, the distribution of slip rates along the NAF in the region of Ismetpasa can be summarized as 1. a rapidly slipping segment east of Ismetpasa extending over 60-70 km with slip rates as high as 20 mm/yr, 2. a shallow locking depth between 8 and 12 km-depth below the segment of Ismetpasa and 3. a locking depth between 15 and 20 km-depth elsewhere (Fig. 2).

## 5 Time-dependent surface slip

We explore time-dependent surface slip as directly measured in the InSAR time series. We apply a similar approach to Dalaison et al. (2021) to extract shallow slip along the NAF from the time series of LOS displacements. We first extract, 500 m-wide, fault perpendicular profiles of LOS displacements every 250 m along the NAF at each acquisition time of each of the three time series on tracks 65, 87 and 167. We then extract the across fault step in LOS displacement and interpolate these values in time and space to combine them into time series of strike slip (i.e. fault parallel slip component) and dip slip (i.e. across fault vertical differential motion).

We show in Figure 3 the space and time evolution of surface slip along the section where aseismic slip has been identified in previous studies. In addition, we apply the deep denoiser developed by Rouet-Leduc et al. (2021) in order to detect the most important variations of surface slip. This denoiser is a trained convolutional neural network specifically designed to remove tropospheric artefacts from time series of LOS apparent displacements. Effectively, the denoiser removes what is identified as noise (i.e. here Gaussian correlated noise, topography correlated phase values and isolated pixels showing anomalous values wrt. their surrounding pixels) and highlights surface displacement consistent with those produced by dislocations embedded in an elastic halfspace. This procedure allows to highlight surface slip that shows a spatial coherence along strike and a temporal consistency. Here, we show the instantaneous slip rate as measured on the output of the denoiser, considering the time spanned by the acquisitions used as input to the neural network. Finally, these results are compared with ground-truth measurements from a local creepmeter (Bilham et al., 2016).

The history of strike slip along the aseismic section extending east of Ismetpasa shows along strike variations. We observe slip rate accelerations and decelerations over a 30 km-long section of the NAF, extending from 10 km west (Lon 32.5°) to 20 km east (Lon 32.85°)

400 of Ismetpasa. Surface slip events lasting a few days to a few weeks can be seen, for in-  
401 stance from km 10 to 20 early 2016. Some of these slip events are also captured by the  
402 creepmeter in Ismetpasa, such as the  $\sim 5$  mm slip events in mid-2017 and late 2020 (Fig.  
403 3). The denoiser detect these two transients, which display similar along-strike length  
404 as the event detected in 2013 by Rousset et al. (2016) and cleaned up by Rouet-Leduc  
405 et al. (2021). Their spatial extent is directly visible in the time series (Fig. S-17 of sup-  
406plementary materials) although it does not stand out clearly enough from the noise to  
407 allow us to model their depth extent. The corresponding denoised surface displacements  
408 is not helpful to constrain the depth extent as the neural network is unable to recover  
409 the long wavelength of a deformation field (Rouet-Leduc et al., 2021).

410 Interestingly, we do not observe transient slip accelerations over the easternmost  
411 section. From 20 to 75 km east of Ismetpasa, we record steady surface slip with no ob-  
412 vious slow slip events. The denoiser neither captures sudden slip accelerations, suggest-  
413 ing that slow slip events are not hidden in the noise of our time series. If occurring, slow  
414 slip events may be too small to be recorded by InSAR. More sensitive, local instruments  
415 such as creep- or strain-meters should be installed.

416 Vertical differential motion across the fault observed in the westernmost section also  
417 does not show sudden accelerations. Potential periodic signals in the vertical differen-  
418 tial motion can be seen in the central section between km 20 and 30, although the cor-  
419 responding variations are small (i.e. less than 4 mm) hence should be taken with cau-  
420 tion. No significant differential vertical motion is observed over the 40 easternmost km  
421 of the section.

## 422 **6 Discussion**

423 As a summary, the central section of the North Anatolian Fault can be character-  
424 ized by the presence of a 60 km-long section that slips continuously since, at least the  
425 1980's (Altay & Sav, 1991). Evidence from the 50's and 70's are local and subject to de-  
426 bate (Ambraseys, 1970; Bilham et al., 2016). Since no significant seismicity is observed  
427 along the section at least since the 60's, slip is considered as mostly aseismic. Slow slip  
428 events are observed every 2.5 years with 5 to 15 mm of slip at the surface over the west-  
429 ernmost part of the aseismic segment. The eastern part of the segment slips continuously  
430 at rates reaching 1 cm/yr, half of the relative plate motion expected at this location. At

431 depth, aseismic slip extends from the surface to a depth of 5 to 6 km. Below, the fault  
432 is locked over a 4 to 5 km-wide portion. The locking depth below this aseismic section  
433 is relatively shallow, 12 km, compared to the 15 to 20 km observed elsewhere along the  
434 fault.

### 435 **6.1 Consistency of creepmeter and InSAR measurements**

436 The first notable element of discussion is the accuracy and precision of both InSAR  
437 data and creepmeter measurements. Creepmeters installed in Ismetpasa measure rela-  
438 tive displacement over a 20 m (Altay & Sav, 1991) or 16.6 m (Bilham et al., 2016) dis-  
439 tance with a 30° angle with respect to the local orientation of the NAF (Altay & Sav,  
440 1991; Bilham et al., 2016). One could argue that these instruments would measure very  
441 local fault slip. Our InSAR data actually show that both the velocity, averaged over sev-  
442 eral years of measurements, and the slow slip events captured by the creepmeters actu-  
443 ally extend for several kilometers along strike. The 2013 slow slip event, even though not  
444 captured by creepmeters as no instrument was installed at the time, is 5-8 km-long and  
445 extends down to 4 km at depth. Events captured by our time series of InSAR data are  
446 of comparable along-strike extent and slip, hence probably a comparable depth extent  
447 although our data is too noisy to allow accurate slip modeling at depth. This means that  
448 the largest events captured by creepmeters are indeed spanning several kilometers at depth  
449 and along-strike.

450 We note that slip events captured by the creepmeter prior to 2016 are neither vis-  
451 ible in our time series, although a slight long term trend is visible, nor detected by our  
452 neural network (Fig. 3). These events could be local and affect a section of the fault too  
453 small to be detected by InSAR. During the 2014-2016 period, only one Sentinel 1 satel-  
454 lite (Sentinel 1-A) was operational and the frequency of SAR acquisitions doubled with  
455 the launched of Sentinel 1-B. The lower sensitivity to mm to cm slip events during the  
456 2014-2016 could also be related to such lower rate of repetition of acquisitions.

457 InSAR time series have 160 m-sized pixels and we evaluate surface slip by linear  
458 regression of the InSAR data over several kilometers on both sides of the fault. There-  
459 fore, the surface slip captured by InSAR is representative of the first kilometers at depth.  
460 The intermediate conclusion here is that this creepmeter captures events spanning a depth  
461 much larger than its across fault extent would lead to consider. We also conclude that,

462 to first order, there is no significant variations in slip at depth during the slow slip events  
463 at Ismetpasa between the surface and a depth of 1 to 2 km.

## 464 **6.2 The rheology of the aseismic section**

465 Comparing results with previously published ones, the along strike distribution of  
466 surface slip rates we infer is comparable to that measured by Cetin et al. (2014) and Kaneko  
467 et al. (2012) with Envisat data over the 2003-2010 period. We observe a gradual increase  
468 in slip rates east of Ismetpasa, reaching up to 1 cm/yr, and a decrease further east over  
469 the 60 km-long segment. The only notable exception is a 10 km-long fast slipping sec-  
470 tion observed by Cetin et al. (2014) in the 2003-2010 data with rates as high as 2 cm/yr,  
471 20 to 30 km east of Ismetpasa. Such high rates have not been described by Kaneko et  
472 al. (2012) with the same data. In addition, we observe that, over the 2014-2020 period,  
473 slip rates to the east of Ismetpasa are remarkably stable with no significant temporal vari-  
474 ations. As no ground-based measurements are available for that part of the fault, we have  
475 to compare InSAR measurements inferred from data acquired by different satellites and  
476 processed with different techniques. For instance, Cetin et al. (2014) used a persistent  
477 scatterer method to process the data and obtained less pixels compared to our SBAS-  
478 like approach but with a potentially higher precision in the velocity measurement. Al-  
479 though it would be tempting to conclude on a local drop in velocity from 2 to 1 cm/yr  
480 in the central part of the section between the periods covered by Envisat data (2001-2010)  
481 and by Sentinel 1 data (2014 onwards), we prefer to remain cautious on this point be-  
482 cause of the inconsistency between measurements by Cetin et al. (2014) and Kaneko et  
483 al. (2012). The relative temporal stability of surface slip over the 2014-2020 period ac-  
484 tually advocates for a stable slip rate over the last 2 decades.

485 Near Ismetpasa, early creepmeter measurements revealed the occurrence of slow slip  
486 events in the 1980's (Altay & Sav, 1991). Comparable accelerations are described by Rousset  
487 et al. (2016) and Bilham et al. (2016) in 2013 and 2014-2016, although with slightly lower  
488 amplitude than during the 1980's. As rightly pointed out by Bilham et al. (2016), alias-  
489 ing of measurements with different and potentially uneven temporal sampling leads to  
490 different conclusions. Over periods of several days, rates vary by one to two orders of mag-  
491 nitude. Averaging over years of measurements, the slip rate at Ismetpasa is remarkably  
492 stable, although a slight decay may be considered (Fig. 4). After a revisit of the mea-  
493 surement of the original wall offset by Ambraseys (1970), Bilham et al. (2016) proposed

494 a corrected estimate of the surface slip rate in the 1960's of 1 cm/yr. In addition, Bilham  
495 et al. (2016) discards the early measurement of an offset in railroad tracks as deemed too  
496 uncertain, in agreement with Ambraseys (1970). Using the corrected slip rates from Bilham  
497 et al. (2016), one may consider a decrease in averaged slip rates (Fig. 3), from 1 cm/yr  
498 in 1970 to  $6\pm 2$  mm/yr in 2020. However, the uncertainty provided with the measure-  
499 ment on the wall photograph from 1969 is of 0.4 mm/yr, a value unrealistically small for  
500 such measurement. Similar concern may be raised for other measurements with uncer-  
501 tainties lower than one mm/yr based on historical photographs. Considering uncertain-  
502 ties might have been underestimated, the decrease in slip rate at Ismetpasa is not ob-  
503 vious anymore.

504 Furthermore, considering that the slip rate estimate inferred by Ambraseys (1970)  
505 for the 1944-1950 time period has been discarded by Bilham et al. (2016) as too uncer-  
506 tain, the hypothesis of a long standing post-seismic decay put forward by Kaneko et al.  
507 (2012) and Cetin et al. (2014) becomes difficult to accept. The expected logarithmic de-  
508 cay of slip rates following a large earthquake is simply not shown by the data as only a  
509 slight decrease in slip rates is visible from 1960 to today. Conditions for such post-seismic  
510 afterslip are the presence of a locked, seismogenic asperity at depth, as confirmed by our  
511 and previously published analysis (e.g. Cetin et al., 2014; Bilham et al., 2016) and the  
512 presence of rate-strengthening material near the surface. The depth-dependence of con-  
513 stitutive parameters of friction laws suggests that rate-strengthening material is to be  
514 expected near the surface (e.g. Blanpied et al., 1991; Scholz, 1998), but is not confirmed  
515 by geodetic data here as no obvious post-seismic signal is observed. We cannot discard  
516 the hypothesis that afterslip occurred after the 1944 earthquake, as would be expected  
517 for such a large earthquake, but we simply cannot reject nor support this hypothesis with  
518 the available data.

519 In addition, rocks exposed at the surface along the aseismic segment include vol-  
520 canic deposits, sedimentary units (limestones) and metamorphic rocks (Cetin et al., 2014),  
521 suggesting no specific link between rock type and slip behavior. Kaduri et al. (2019) pro-  
522 pose a relationship between the development of a specific mineralogical fabric in the fault  
523 material and the occurrence of aseismic slip. The peculiar slip behavior of this segment,  
524 compared to the rest of the NAF that ruptured during the 1944 earthquake, cannot be  
525 explained by fault material composition but aseismic slip instead seems related to the  
526 occurrence of pressure solution creep. Similar observations have been made along the

527 Longitudinal Valley fault in Taiwan and the San Andreas Fault in California (Thomas  
528 et al., 2014; Gratier et al., 2011).

529 Finally, it is important to realize that all reports of aseismic slip published to date  
530 focused on the surroundings of the city of Ismetpasa, to the exception of Cetin et al. (2014)  
531 and Kaneko et al. (2012). At this peculiar location, as pointed out earlier by Aytun (1982),  
532 we observe vertical differential motion across the fault, consistent with subsidence mea-  
533 sured north of the fault near Ismetpasa. Such subsidence is probably related to hydro-  
534 logical effects. Therefore, the slip behavior of the NAF in Ismetpasa is not representa-  
535 tive of that of the entire creeping section.

536 All in all, it is difficult to conclude firmly on the rheology of fault material along  
537 this aseismic section. Aseismic slip seems steady since at least the 1960's to the excep-  
538 tion of the peculiar location of Ismetpasa. If further evidence of post-seismic slip follow-  
539 ing the 1944 earthquake were to be put forward, then an effective rate-strengthening rhe-  
540 ology should be considered. In such case, slow slip events in Ismetpasa can be explained  
541 by the presence of small heterogeneities in frictional constitutive properties (Wei et al.,  
542 2013). Without any additional evidence, fault rheology is still a matter of debate as aseis-  
543 mic slip may result from a large nucleation size, geometrical complexities or low normal  
544 stress conditions. For instance, in the case of rate-weakening properties, reduced nor-  
545 mal stress results in a large nucleation size hence promotes slow slip and spontaneous  
546 slow slip events may occur at the transition between locked and creeping regions (e.g.  
547 Liu & Rice, 2005).

### 548 **6.3 A simple, testable explanation for shallow aseismic slip**

549 Although the lack of evidence to constrain the rheology of fault material in this re-  
550 gion might be disappointing, the geometry of the distribution of aseismic slip at depth  
551 may provide an explanation for the occurrence of shallow slip in this region. As shown  
552 by our model, the locking depth below the aseismic slip segment is shallower than else-  
553 where along the fault (Fig. 2). Such shallow locking depth is actually the only feature  
554 that differentiates the creeping segment from the rest of the fault covered by our study.  
555 This particular is highlighted by the characteristic pattern of surface displacement rates,  
556 showing a gradual change in velocity approaching the fault (Fig. S-13 of supplementary  
557 materials). This bending, visible between 10 km away from the fault and the fault trace,

558 is interpreted as the signature of elastic stress build up on a locked asperity. Since the  
 559 fault slips at the surface, as highlighted by the step-like change in surface velocity across  
 560 the fault, this locked asperity must be located between the locking depth and the bot-  
 561 tom of the creeping zone.

562 Shallow locking depth results in higher stressing rates at the surface. For a semi-  
 563 infinite dislocation embedded in an elastic halfspace buried at a depth  $d$ , shear stress-  
 564 ing rate,  $\dot{\tau}$ , at the surface writes as  $\dot{\tau} = \frac{\mu\dot{\delta}}{2\pi d}$  with  $\mu$  the shear modulus and  $\dot{\delta}$  the slip  
 565 rate on the fault. Assuming a constant shear modulus and slip rates, shallowing the lock-  
 566 ing depth  $d$  from 20 to 10 km results in a twofold increase in stressing rate. For instance,  
 567 with a 2 cm/yr slip rate and a 30 GPa shear modulus, shear stressing rate at the sur-  
 568 face jumps from approximately 5 to 10 kPa/yr. Alone, such change in shear stressing  
 569 rate should not lead to any change in slip behavior.

570 Whether shallow fault material is rate-weakening or -strengthening, the depth-distribution  
 571 of effective normal stress, the difference between normal stress and pore pressure, influ-  
 572 ences frictional resistance. Low normal stress implies slip occurs at lower stress for a given  
 573 coefficient of friction. Then, if shallow fault material is rate-strengthening, a higher (resp.  
 574 lower) shear stressing rate should lead to the occurrence of constant shallow slow slip  
 575 earlier (resp. later) in the between two large earthquakes. If shallow fault material is rate-  
 576 weakening, we must consider the depth-distribution of nucleation size.

577 Nucleation size is inversely proportional to normal stress (e.g. Ampuero & Rubin,  
 578 2008) and large nucleation size leads to conditionally stable slip. If the nucleation size  
 579 is larger than the size of the fault, then slip cannot become dynamic and slip rates will  
 580 remain slow. Effective normal stress results from the combination of overburden and pore  
 581 pressure. To first order, normal stress increases linearly with depth, controlled by the  
 582 density of crustal rocks. Considering the evolution of permeability with normal stress,  
 583 it can be shown that effective normal stress increases with overburden until a depth of  
 584 3 to 5 km, depth below which normal stress becomes constant (Rice, 1992). In both cases,  
 585 there is a lowering of normal stress at the surface and the depth distribution of normal  
 586 stress results in a variation in nucleation size inversely proportional to depth, with max-  
 587 imum nucleation size at the surface. Considering such depth distribution of nucleation  
 588 size is constant along strike, a local shallowing of the locking depth resulting in an in-

589 crease in shear stressing rate at the surface would potentially increase slip rate at the  
590 surface while keeping slip to sub-dynamic speed (i.e. slow).

591 In both rate-strengthening or -weakening shallow fault material, a shallow (resp.  
592 deep) locking depth may result in faster (resp. slower) surface slip rates. In particular,  
593 such hypothesis does not involve any along strike variations of rheology or fluid content  
594 as only the shallowing of the locking depth is involved. Under these conditions, a homo-  
595 geneous along strike fault rheology would be sufficient to explain spatial and temporal  
596 variations in surface aseismic slip rates. This hypothesis should now be evaluated care-  
597 fully as other parameters may play a role, such as the constitutive parameters or the evo-  
598 lution of stresses in between two large earthquakes. Obviously, a physical explanation  
599 to a local variation in locking depth is unfortunately missing.

## 600 **7 Conclusion**

601 We provide 100 m-scale resolution time series of surface displacement across the  
602 North Anatolian Fault from Sentinel 1 InSAR data in order to explore the details of the  
603 spatial and temporal distribution of aseismic slip along the creeping section of Ismetpasa.  
604 We confirm the presence of aseismic slip over the shallow portion of the fault (surface  
605 to 5 km-depth), colocated with a shallow locking depth (10-12 km-depth). Our surface  
606 displacement data is elsewhere compatible with a 15-20 km-depth. Current conclusions  
607 suggest that the evidence put forward to sustain the notion of long lasting afterslip fol-  
608 lowing the 1944 earthquake are subject to debate, which, unfortunately, does not allow  
609 to conclude firmly on the rheology of the fault at shallow depth. Although our data can-  
610 not exclude a generic depth-dependent behavior of the relationship between slip rate and  
611 friction, the occurrence of slow slip events and the variability of rocks exposed at the sur-  
612 face forces to consider that rock type, hence constitutive properties, might not be the  
613 primary control on the presence of aseismic slip along this fault segment. Otherwise, one  
614 would need to consider the occurrence of shallow slow slip all along the fault, where large,  
615  $M_w > 7$  earthquakes have occurred over the 20th century. We propose that shallow lock-  
616 ing depth plays a role, although further investigations are needed to explain such par-  
617 ticular feature.

**Acknowledgments**

618  
619 The authors would like to thank Dr Harsha S. Bhat, Dr Cécile Lasserre, Pr. Pierre Dublanchet  
620 and Pr. Dmitry Garagash for insightful discussions. This project has received funding  
621 from the European Research Council (ERC) under the European Union's Horizon 2020  
622 research and innovation program (Grant Agreements 758210 for project Geo4D). Romain  
623 Jolivet acknowledges funding from the Institut Universitaire de France. We thank the  
624 European Space Agency for the acquisition and the distribution of the SAR data by the  
625 Sentinel 1 constellation (may it fly forever and ever). InSAR data are available for down-  
626 load here: <https://peps.cnes.fr/>. ERA-Interim products are directly available for down-  
627 load at ECMWF (<https://www.ecmwf.int/>). InSAR data have been processed using  
628 the ISCE framework (<https://github.com/isce-framework/isce2>). Creepmeter data  
629 have been downloaded at the Unavco repository for geodetic data ([https://www.unavco](https://www.unavco.org/data/strain-seismic/creep-data/creep-data.html)  
630 [.org/data/strain-seismic/creep-data/creep-data.html](https://www.unavco.org/data/strain-seismic/creep-data/creep-data.html)). IGS data are available  
631 here <http://www.igs.org>. GNSS data from the Turkish national network are available  
632 here: <https://www.tusaga-aktif.gov.tr/>. Data collected in the field with out sta-  
633 tions along the North Anatolian Fault have been uploaded at <http://osf.io/9t3n7>.  
634 Modeling has been conducted using elements of the Classic Slip Inversion library ([https://](https://github.com/jolivet/csi)  
635 [github.com/jolivet/csi](https://github.com/jolivet/csi)) and AlTar (<https://github.com/AlTarFramework/altar>).  
636 Notebooks detailing the procedure will be made available on Romain Jolivet's personal  
637 webpage.

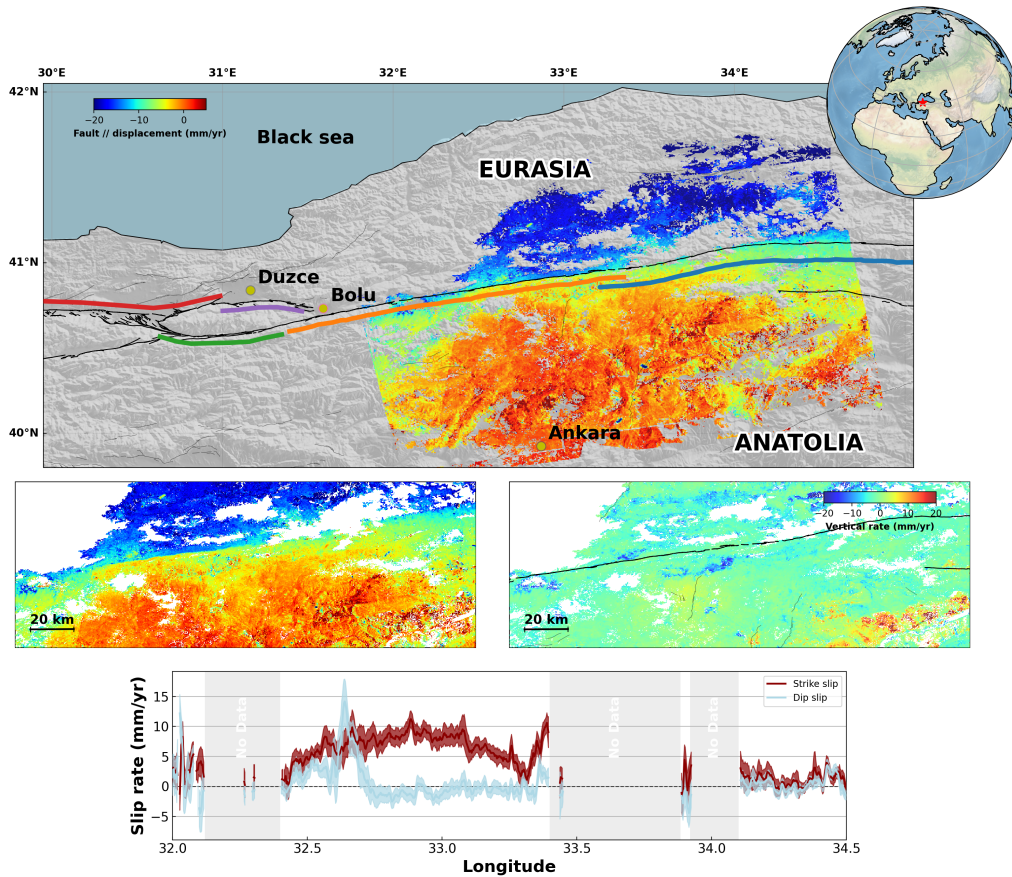


**Figure 1. Fault parallel velocity map, vertical velocity map and surface slip** - Top panel: Color indicates the fault parallel velocity derived from the combination of velocity maps on Sentinel 1 ascending and descending tracks. Dark lines indicate the main trace of the North Anatolian Fault. Grey lines are secondary faults. Colored lines indicate the along strike extent of large historical and recent earthquakes including the 1943  $M_w$  7.6 Tosia-Ladik earthquake (blue), the 1944  $M_w$  7.3 Bolu-Gerede earthquake (orange), the 1967  $M_w$  7.2 Mudurnu earthquake (green), the 1999  $M_w$  7.6 Izmit earthquake (red) and the 1999  $M_w$  7.2 Düzce earthquake (purple). Center-left panel is a zoom on the area where aseismic slip is most visible, extending over the entire creeping section. Center-right panel shows the vertical displacement rate over that same area (positive is uplift). Lower panel shows surface slip rate along the fault as measured on the InSAR velocity maps. Red is strike slip while light blue is dip slip (i.e. effectively differential vertical motion at the fault trace). Grey shading shows areas of low coherence and data is missing.

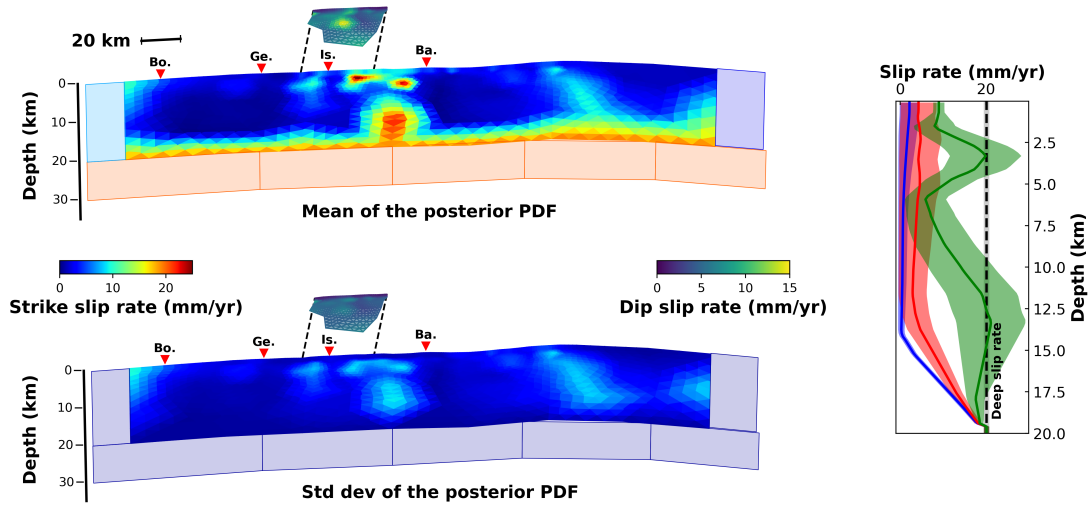


**Figure 2. Fault slip distribution and uncertainties - Top** Mean of the posterior Probability Density Function of slip rate (strike slip). Rectangles on the side represent the dislocations used to model the western and eastern extension of the fault model as well as the deep dislocation modeling the far field displacement rate. Note that these dislocations extend sideways and at depth as semi-infinite structures. Small fault structure offset from the main fault shows the distribution of dip slip rate in the vicinity of the subsiding north of the city of Ismetpasa. Red triangles are cities located along the fault, including Bolu (Bo.), Gerede (Ge.), Ismetpasa (Is.) and Bayamoren (Ba.). **Bottom** Standard deviation of the slip rate (strike slip and dip slip) posterior PDF. **Right** Depth distribution of slip rate with associated uncertainties at longitude 31.9 (blue), 32.9 (green) and 33.9 (red). Longitude 32.9 is within the creeping section. Dark dashed line is the deep slip rate. The effective locking depth within the creeping section is inferred somewhere between 10 and 12.5 km depth.

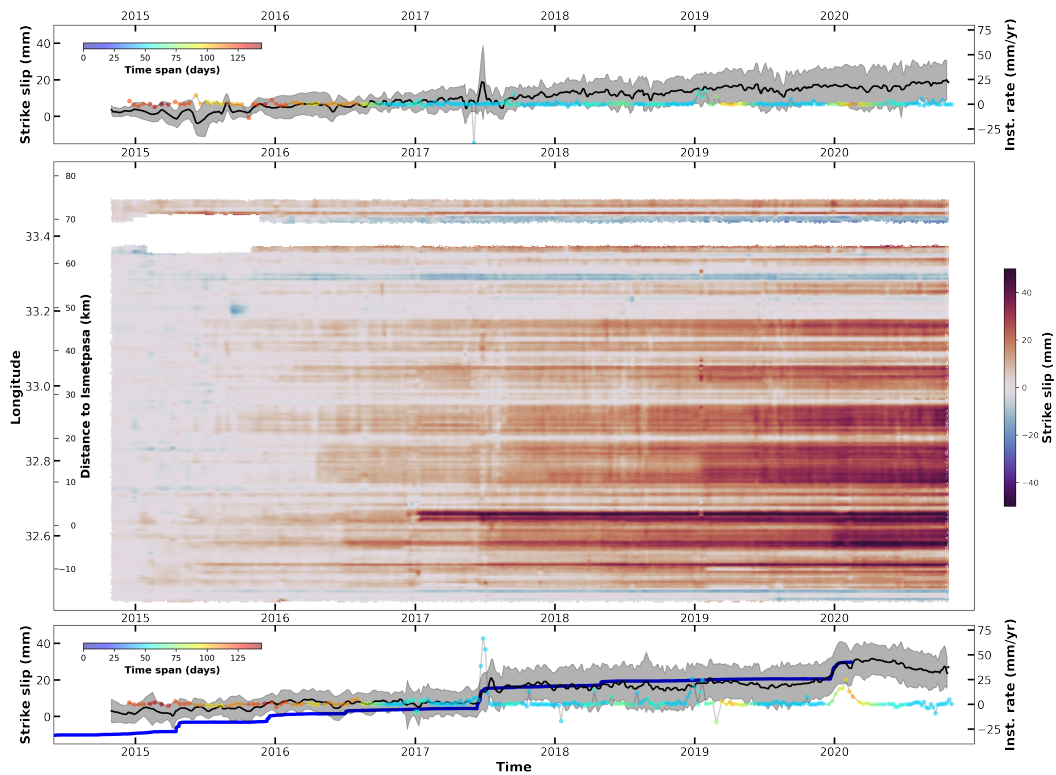


**Figure 3. Time dependent surface slip rate** - Space and time dependent surface slip rate (strike slip) obtained from regularly spaced profiles (see supp. mat.) Y-axis is labeled as a function on longitude and distance to Ismetpassa. Top and bottom plots show the time evolution of surface slip (dark) with the associated uncertainties (gray shading) at two distinct locations, including the Ismetpassa train station (bottom) and at  $33.1^{\circ}\text{N}$ (top). Colored dots indicate the slip rate measured on sets of 9 consecutive acquisitions cleaned from atmospheric noise with a convolutional neural net (Rouet-Leduc et al., 2021). Color indicates the time span of the 9 acquisitions. Blue line is the strike slip measured by the creepmeter installed at the Ismetpassa train station Bilham et al. (2016).

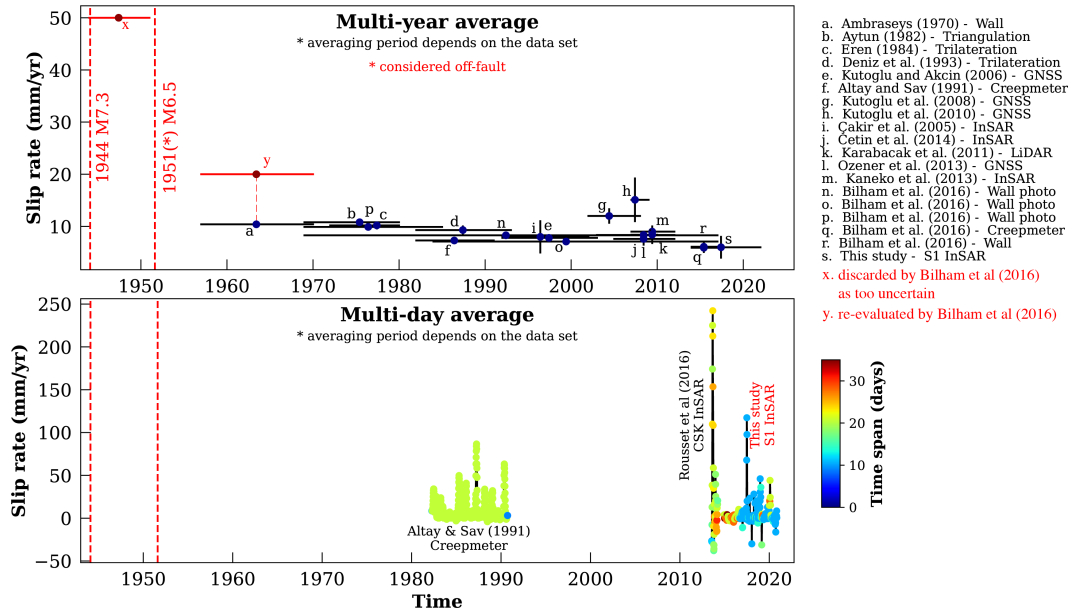


**Figure 4.** Evolution of surface aseismic slip rate at Isetmpasa - Surface slip rates averaged over several years (top) and over variable but day-to-week time scales (bottom). Colored dots indicate the time span over which slip rate has been estimated. Red dashed lines indicate the time of occurrence of the 1944  $M_w$  7.3 Bolu-Gerede and the 1951  $M_w$  6.5 Isetmpasa earthquakes. Rates are from Ambraseys (1970), Aytun (1982), Eren (1984), Deniz et al. (1993), Altay and Sav (1991), Çakir et al. (2005), Kutoglu and Akcin (2006), Kutoglu et al. (2008), Kutoglu et al. (2010), Karabacak et al. (2011), Deguchi (2011), Ozener et al. (2013) and Kaneko et al. (2012). Some rates were re-evaluated by Bilham et al. (2016).

638 **References**

- 639 Agram, P. S., Jolivet, R., Riel, B., Lin, Y. N., Simons, M., Hetland, E., . . . Lasserre,  
 640 C. (2013). New Radar Interferometric Time Series Analysis Toolbox Released.  
 641 *Eos*, *94*(7), 69–76. Retrieved from [http://www.agu.org/pubs/crossref/](http://www.agu.org/pubs/crossref/2012/2011JB008731.shtml)  
 642 [2012/2011JB008731.shtml](http://www.agu.org/pubs/crossref/2012/2011JB008731.shtml) doi: 10.1029/2011JB008731
- 643 Altamimi, Z., Rebischung, P., Métivier, L., & Collilieux, X. (2016). ITRF2014: A  
 644 new release of the International Terrestrial Reference Frame modeling nonlin-  
 645 ear station motions. *Journal of Geophysical Research: Solid Earth*, *121*(8),  
 646 6109–6131. doi: 10.1002/2016JB013098
- 647 Altay, C., & Sav, H. (1991). Continuous creep measurement along the North Anato-  
 648 lian Fault zone. *Bulletin of the geological congres of Turkey*, *6*, 77–84.
- 649 Ambraseys, N. N. (1970). Some characteristic features of the Anatolian fault zone.  
 650 *Tectonophysics*, *9*, 143–165.
- 651 Ampuero, J.-P., & Rubin, A. M. (2008). Earthquake nucleation on rate and state  
 652 faults – Aging and slip laws. *Journal of Geophysical Research*, *113*(B1),  
 653 B01302–21. doi: 10.1029/2007JB005082
- 654 Avouac, J.-P. (2015). From Geodetic Imaging of Seismic and Aseismic Fault Slip  
 655 to Dynamic Modeling of the Seismic Cycle. *Annual Review of Earth and Plan-  
 656 etary Sciences*, *43*(1), 233–271. doi: 10.1146/annurev-earth-060614-105302
- 657 Aytun, A. (1982). Creep Measurements in the Ismetpaşa Region of the North  
 658 Anatolian Fault Zone. *Multidisciplinary Approach to Earthquake Prediction  
 659 Progress in Earthquake Prediction Research*, *2*, 279–292.
- 660 Barbot, S., & Weiss, J. R. (2021). Connecting subduction, extension, and shear  
 661 localization across the aegean sea and anatolia. *Geophysical Journal Interna-  
 662 tional*, *226*(1), 422–445. doi: 10.1093/gji/ggab078
- 663 Barka, A. (1996). Slip distribution along the north anatolian fault associated with  
 664 the large earthquakes of the period 1939 to 1967. *Bulletin of the Seismological  
 665 Society of America*, *86*(5), 1238–1254.
- 666 Benoit, A., Pinel-Puysssegur, B., Jolivet, R., & Lasserre, C. (2020). CorPhU: an  
 667 algorithm based on phase closure for the correction of unwrapping errors in  
 668 SAR interferometry. *Geophysical Journal International*, *221*(3), 1959–1970.  
 669 doi: 10.1093/gji/ggaa120
- 670 Bevis, M., & Brown, A. (2014). Trajectory models and reference frames for crustal

- 671 motion geodesy. *Journal of Geodesy*, *88*(3), 283–311. doi: 10.1007/s00190-013  
672 -0685-5
- 673 Bilham, R., Ozener, H., Mencin, D., Dogru, A., ERGINTAV, S., ÇAKIR, Z., ...  
674 Mattioli, G. (2016). Surface creep on the North Anatolian Fault at Ismetpasa,  
675 Turkey, 1944-2016. *Journal of Geophysical Research-Solid Earth*, *121*, 7409–  
676 7431. doi: 10.1002/2016JB013394
- 677 Blanpied, M. L., Lockner, D. A., & Byerlee, J. D. (1991). Fault stability inferred  
678 from granite sliding experiments at hydrothermal conditions. *Geophysical Re-*  
679 *search Letters*, *18*(4), 609–612. doi: 10.1029/91GL00469
- 680 Bletery, Q., Cavalié, O., Nocquet, J.-M., & Ragon, T. (2020). Distribution of inter-  
681 seismic coupling along the north and east anatolian faults inferred from insar  
682 and gps data. *Geophysical Research Letters*, *47*(16), e2020GL087775. doi:  
683 10.1029/2020GL087775
- 684 Bouchon, M., Karabulut, H., Aktar, M., Ozalaybey, S., Schmittbuhl, J., & Bouin,  
685 M. P. (2011). Extended Nucleation of the 1999 Mw 7.6 Izmit Earthquake.  
686 *Science*, *331*(6019), 877–880. doi: 10.1126/science.1197341
- 687 Bürgmann, R. (2018). The geophysics, geology and mechanics of slow fault slip.  
688 *Earth and Planetary Science Letters*, *495*, 112–134. doi: 10.1016/j.epsl.2018.04  
689 .062
- 690 Çakir, Z., Akoglu, A., Belabbes, S., Ergintav, S., & Meghraoui, M. (2005). Creeping  
691 along the Ismetpasa section of the North Anatolian fault (Western Turkey):  
692 Rate and extent from InSAR. *Earth and Planetary Science Letters*, *238*(1-2),  
693 225–234. doi: 10.1016/j.epsl.2005.06.044
- 694 Candela, T., Renard, F., Klinger, Y., Mair, K., Schmittbuhl, J., & Brodsky, E. E.  
695 (2012). Roughness of fault surfaces over nine decades of length scales. *Journal*  
696 *of Geophysical Research*, *117*(B8), B08409. doi: 10.1029/2011JB009041
- 697 Cattania, C., & Segall, P. (2021). Precursory slow slip and foreshocks on rough  
698 faults. *Journal of Geophysical Research: Solid Earth*, *126*(4), e2020JB020430.  
699 doi: 10.1029/2020JB020430
- 700 Cetin, E., Cakir, Z., Meghraoui, M., Ergintav, S., & Akoglu, A. M. (2014). Extent  
701 and distribution of aseismic slip on the Ismetpaşa segment of the North Anato-  
702 lian Fault (Turkey) from Persistent Scatterer InSAR. *Geochemistry Geophysics*  
703 *Geosystems*, *15*(7), 2883–2894. doi: 10.1002/2014GC005307

- 704 Dalaison, M., & Jolivet, R. (2020). A kalman filter time series analysis method for  
 705 insar. *Journal of Geophysical Research: Solid Earth*, *125*(7), e2019JB019150.  
 706 doi: 10.1029/2019JB019150
- 707 Dalaison, M., Jolivet, R., van Rijsingen, E. M., & Michel, S. (2021). The interplay  
 708 between seismic and aseismic slip along the chaman fault illuminated by insar.  
 709 *Journal of Geophysical Research: Solid Earth*, *126*(12), e2021JB021935. doi:  
 710 10.1029/2021JB021935
- 711 Deguchi. (2011). Detection of fault creep around naf by insar time series analysis  
 712 using palsar data. *Proc. of SPIE, SAR Image Analysis, Modeling, and Tech-*  
 713 *niques XI*, 8179. doi: 10.1117/12.898478
- 714 DeMets, C., Gordon, R. G., & Argus, D. F. (2010). Geologically current plate mo-  
 715 tions. *Geophysical Journal International*, *181*(1), 1–80. doi: 10.1111/j.1365-  
 716 -246X.2009.04491.x
- 717 den Hartog, S. A. M., & Spiers, C. J. (2013). Influence of subduction zone condi-  
 718 tions and gouge composition on frictional slip stability of megathrust faults.  
 719 *Tectonophysics*, *600*, 75–90. doi: 10.1016/j.tecto.2012.11.006
- 720 Deniz, R., Aksoy, A., Yalin, D., Seeger, H., Franke, P., Hirsch, O., & Bautsch,  
 721 P. (1993). Determination of crustal movements in turkey by terres-  
 722 trial geodetic methods. *Journal of Geodynamics*, *18*(1), 13–22. doi:  
 723 [https://doi.org/10.1016/0264-3707\(93\)90024-Z](https://doi.org/10.1016/0264-3707(93)90024-Z)
- 724 Dettmer, J., Benavente, R., Cummins, P. R., & Sambridge, M. (2014). Trans-  
 725 dimensional finite-fault inversion. *Geophysical Journal International*, *199*(2),  
 726 735–751. doi: 10.1093/gji/ggu280
- 727 Dianala, J. D. B., Jolivet, R., Thomas, M. Y., Fukushima, Y., Parsons, B., &  
 728 Walker, R. (2020). The relationship between seismic and aseismic slip on the  
 729 philippine fault on leyte island: Bayesian modeling of fault slip and geother-  
 730 mal subsidence. *Journal of Geophysical Research: Solid Earth*, *125*(12),  
 731 e2020JB020052. doi: 10.1029/2020JB020052
- 732 Dragert, H., Wang, K., & Thomas, J. S. (2001). A Silent Slip Event on the Deeper  
 733 Cascadia Subduction Interface. *Science*, *292*(5521), 1525–1528. doi: 10.1126/  
 734 science.1060152
- 735 Duputel, Z., Agram, P. S., Simons, M., Minson, S. E., & Beck, J. L. (2014). Ac-  
 736 counting for prediction uncertainty when inferring subsurface fault slip. *Geo-*

- 737 *physical Journal International*, 197(1), 464–482. doi: 10.1093/gji/ggt517
- 738 Duquesnoy, T., Barrier, E., Kasser, M., Aurelio, M., Gaulon, R., Punongbayan,  
739 R. S., & Rangin, C. (1994). Detection of creep along the Philippine fault:  
740 First results of geodetic measurements on Leyte island, central Philippine.  
741 *Geophysical Research Letters*, 21(11), 975–978. doi: 10.1029/94GL00640
- 742 Ellsworth, W. L., & Bulut, F. (2018). Nucleation of the 1999 Izmit earthquake by  
743 a triggered cascade of foreshocks. *Nature Geoscience*, 84, 1–6. doi: 10.1038/  
744 s41561-018-0145-1
- 745 Eren, K. (1984). Strain analysis along the north anatolian fault by using geodetic  
746 surveys. *Bulletin géodésique*, 58(2), 137–150. doi: 10.1007/BF02520898
- 747 Fattahi, H., Agram, P., & Simons, M. (2016). A Network-Based Enhanced Spec-  
748 tral Diversity Approach for TOPS Time-Series Analysis. *IEEE Transactions*  
749 *on Geoscience and Remote Sensing*, 55(2), 777–786. doi: 10.1109/TGRS.2016  
750 .2614925
- 751 Goldstein, R. M., & Werner, C. L. (1998, November). Radar interferogram filtering  
752 for geophysical applications. *Geophysical Research Letters*, 25(21), 4035–4038.
- 753 Goldstein, R. M., Zebker, H. A., & Werner, C. L. (1988). Satellite radar interferome-  
754 try: Two-dimensional phase unwrapping. *Radio Science*, 23(4), 713–720.
- 755 Gratier, J. P., Richard, J., Renard, F., Mitterpergher, S., Doan, M. L., Di Toro,  
756 G., . . . Boullier, A. M. (2011). Aseismic sliding of active faults by pressure  
757 solution creep: Evidence from the San Andreas Fault Observatory at Depth.  
758 *Geology*, 39(12), 1131–1134. doi: 10.1130/G32073.1
- 759 Gurrola, E., Rosen, P., Sacco, G., Seliga, W., Zebker, H., Simons, M., & Sandwell,  
760 D. (2010). Sar scientific computing environment. In *Paper presented at the*  
761 *american geophysical union fall meeting, san francisco, ca.*
- 762 Herring, T. A., King, R., Floyd, M., & McClusky, S. C. (2018). GAMIT Reference  
763 Manual. GPS Analysis at MIT GLOBK, Release 10.7. (June), 168.
- 764 Jolivet, R., Agram, P. S., Lin, N. Y., Simons, M., Doin, M.-P., Peltzer, G., & Li,  
765 Z. (2014). Improving InSAR geodesy using Global Atmospheric Mod-  
766 els. *Journal of Geophysical Research-Solid Earth*, 119(3), 2324–2341. doi:  
767 10.1002/2013JB010588
- 768 Jolivet, R., Candela, T., Lasserre, C., Renard, F., Klinger, Y., & Doin, M. P. (2015).  
769 The Burst-Like Behavior of Aseismic Slip on a Rough Fault: The Creeping

- 770 Section of the Haiyuan Fault, China. *Bulletin of the Seismological Society of*  
 771 *America*, 105(1), 480–488. doi: 10.1785/0120140237
- 772 Jolivet, R., & Frank, W. B. (2020). The Transient and Intermittent Nature of Slow  
 773 Slip. *AGU Advances*, 1(1), e2019AV000126–8. doi: 10.1029/2019AV000126
- 774 Jolivet, R., Grandin, R., Lasserre, C., Doin, M. P., & Peltzer, G. (2011). Systematic  
 775 InSAR tropospheric phase delay corrections from global meteorological reanal-  
 776 ysis data. *Geophysical Research Letters*, 38(17). doi: 10.1029/2011GL048757
- 777 Jolivet, R., Simons, M., Agram, P. S., Duputel, Z., & Shen, Z. K. (2015). Aseismic  
 778 slip and seismogenic coupling along the central San Andreas Fault. *Geophysical*  
 779 *Research Letters*, 42(2), 297–306. doi: 10.1002/2014GL062222
- 780 Kaduri, M., Gratier, J.-P., Lasserre, C., Çakir, Z., & Renard, F. (2019). Quanti-  
 781 fying the partition between seismic and aseismic deformation along creeping  
 782 and locked sections of the north anatolian fault, turkey. *Pure and Applied*  
 783 *Geophysics*, 176(3), 1293–1321. doi: 10.1007/s00024-018-2027-2
- 784 Kaneko, Y., Avouac, J.-P., & Lapusta, N. (2010). Towards inferring earthquake pat-  
 785 terns from geodetic observations of interseismic coupling. *Nature Geoscience*,  
 786 3(5), 363–369. doi: 10.1038/ngeo843
- 787 Kaneko, Y., Fialko, Y., Sandwell, D. T., Tong, X., & Furuya, M. (2012). Interseis-  
 788 mic deformation and creep along the central section of the North Anatolian  
 789 fault (Turkey): InSAR observations and implications for rate-and-state friction  
 790 properties. *Journal of Geophysical Research-Solid Earth*, 118, 316–331. doi:  
 791 10.1029/2012JB009661
- 792 Karabacak, V., Altunel, E., & Cakir, Z. (2011). Monitoring aseismic surface creep  
 793 along the north anatolian fault (turkey) using ground-based lidar. *Earth and*  
 794 *Planetary Science Letters*, 304(1), 64–70. doi: 10.1016/j.epsl.2011.01.017
- 795 Khoshmanesh, M., & Shirzaei, M. (2018). Multiscale Dynamics of Aseismic Slip on  
 796 Central San Andreas Fault. *Geophysical Research Letters*, 45(5), 2274–2282.  
 797 doi: 10.1002/2018GL077017
- 798 Kodaira, S., Iidaka, T., Kato, A., Park, J.-O., Iwasaki, T., & Kaneda, Y. (2004).  
 799 High pore fluid pressure may cause silent slip in the nankai trough. *Science*,  
 800 304(5675), 1295–1298. doi: 10.1126/science.1096535
- 801 Kondo, H., Awata, Y., Emre, Ö., Doğan, A., Özalp, S., Tokay, F., . . . Okumura, K.  
 802 (2005). Slip distribution, fault geometry, and fault segmentation of the 1944

- 803 bolu-gerede earthquake rupture, north anatolian fault, turkey. *Bulletin of the*  
 804 *Seismological Society of America*, 95(4), 1234–1249. doi: 10.1785/0120040194
- 805 Kondo, H., Özaksoy, V., & Yildirim, C. (2010). Slip history of the 1944 bolu-gerede  
 806 earthquake rupture along the north anatolian fault system: Implications for  
 807 recurrence behavior of multisegment earthquakes. *Journal of Geophysical*  
 808 *Research: Solid Earth*, 115(B4). doi: 10.1029/2009JB006413
- 809 Kutoglu, H. S., & Akcin, H. (2006). Determination of the 30-year creep trend on the  
 810 ismetpaşa segment of the north anatolian fault using an old geodetic network.  
 811 *Earth, Planets and Space*, 58(8), 937–942. doi: 10.1186/BF03352598
- 812 Kutoglu, H. S., Akcin, H., Gundogdu, O., Gormus, K. S., & Koksalsal, E. (2010, 12).  
 813 Relaxation on the ismetpasa segment of the north anatolian fault after the  
 814 golcuk  $m_w = 7.4$  and duzce  $m_w = 7.2$  shocks. *Nat. Hazards Earth Syst. Sci.*,  
 815 10(12), 2653–2657. doi: 10.5194/nhess-10-2653-2010
- 816 Kutoglu, H. S., Akcin, H., Kemaldere, H., & Gormus, K. S. (2008, 12). Triggered  
 817 creep rate on the ismetpasa segment of the north anatolian fault. *Nat. Hazards*  
 818 *Earth Syst. Sci.*, 8(6), 1369–1373. doi: 10.5194/nhess-8-1369-2008
- 819 Liu, Y., & Rice, J. R. (2005). Aseismic slip transients emerge spontaneously in  
 820 three-dimensional rate and state modeling of subduction earthquake sequences.  
 821 *Journal of Geophysical Research: Solid Earth (1978–2012)*, 110(B8), 609–14.  
 822 doi: 10.1029/2004JB003424
- 823 Lohman, R. B., & Simons, M. (2005). Some thoughts on the use of InSAR  
 824 data to constrain models of surface deformation: Noise structure and data  
 825 downsampling. *Geochemistry, Geophysics, Geosystem*, 6(1), Q01007. doi:  
 826 10.1029/2004GC000841
- 827 Maurer, J., & Johnson, K. (2014). Fault coupling and potential for earthquakes on  
 828 the creeping section of the central San Andreas Fault. *Journal of Geophysical*  
 829 *Research*, 119(5), 2013JB010741–4428. doi: 10.1002/2013JB010741
- 830 Mazzotti, S., Le Pichon, X., Henry, P., & Miyazaki, S.-I. (2000). Full interseismic  
 831 locking of the Nankai and Japan-west Kurile subduction zones: An analysis  
 832 of uniform elastic strain accumulation in Japan constrained by permanent  
 833 GPS. *Journal of Geophysical Research: Solid Earth (1978–2012)*, 105(B6),  
 834 13159–13177. doi: 10.1029/2000JB900060
- 835 Minson, S. E., Simons, M., & Beck, J. L. (2013). Bayesian inversion for finite fault

- 836 earthquake source models I—theory and algorithm. *Geophysical Journal Inter-*  
 837 *national*, 194(3), 1701–1726. doi: 10.1093/gji/ggt180
- 838 Mogi, K. (1958). Relations between the Eruptions of Various Volcanoes and the De-  
 839 formation of the Ground Surface around them. *Bulleting of the Earthquake Re-*  
 840 *search Institute*, 36, 99–134.
- 841 Moreno, M., Haberland, C., Oncken, O., Rietbrock, A., Angiboust, S., & Heidbach,  
 842 O. (2014). Locking of the Chile subduction zone controlled by fluid pres-  
 843 sure before the 2010 earthquake. *Nature Geoscience*, 7(4), 292–296. doi:  
 844 10.1038/ngeo2102
- 845 Nocquet, J. (2018). *Pyacs: A set of python tools for gps analysis and tectonic mod-*  
 846 *elling*. 19th General Assembly of Wegener.
- 847 Nocquet, J. M. (2018). Stochastic static fault slip inversion from geodetic data  
 848 with non-negativity and bound constraints. *Geophysical Journal International*,  
 849 214(1), 366–385. doi: 10.1093/gji/ggy146
- 850 Ozener, H., Dogru, A., & Turgut, B. (2013). Quantifying aseismic creep on  
 851 the ismetpasa segment of the north anatolian fault zone (turkey) by 6  
 852 years of gps observations. *Journal of Geodynamics*, 67, 72–77. doi:  
 853 10.1016/j.jog.2012.08.002
- 854 Reid, H. F. (1911). The elastic rebound theory of earthquakes. *Univ. Calif. Publ.*  
 855 *Bull. Dept. Geol.*, 6, 413–444.
- 856 Rice, J. R. (1992). Fault stress states, pore pressure distributions, and the weak-  
 857 ness of the san andreas fault. In B. Evans & T.-F. Wong (Eds.), *Fault mechan-*  
 858 *ics and transport properties in rocks* (p. 475–503). Academic Press.
- 859 Romanet, P., Bhat, H. S., Jolivet, R., & Madariaga, R. (2018). Fast and Slow Slip  
 860 Events Emerge Due to Fault Geometrical Complexity. *Geophysical Research*  
 861 *Letters*, 45(10), 4809–4819. doi: 10.1029/2018GL077579
- 862 Rouet-Leduc, B., Jolivet, R., Dalaison, M., Johnson, P. A., & Hulbert, C. (2021).  
 863 Autonomous extraction of millimeter-scale deformation in insar time se-  
 864 ries using deep learning. *Nature Communications*, 12(1), 6480. doi:  
 865 10.1038/s41467-021-26254-3
- 866 Rousset, B., Jolivet, R., Simons, M., Lasserre, C., Riel, B., Milillo, P., . . . Renard, F.  
 867 (2016). An aseismic slip transient on the North Anatolian Fault. *Geophysical*  
 868 *Research . . .*, 43(7), 3254–3262. doi: 10.1002/2016GL068250

- 869 Ruiz, S., Metois, M., Fuenzalida, A., Ruiz, J., Leyton, F., Grandin, R., ... Cam-  
870 pos, J. (2014). Intense foreshocks and a slow slip event preceded the  
871 2014 Iquique Mw 8.1 earthquake. *Science*, *345*(6201), 1165–1169. doi:  
872 10.1126/science.1256074
- 873 Ryder, I., & Bürgmann, R. (2008, December). Spatial variations in slip deficit on  
874 the central San Andreas Fault from InSAR. *Geophysical Journal Interna-*  
875 *tional*, *175*(3), 837–852. Retrieved from [http://doi.wiley.com/10.1111/](http://doi.wiley.com/10.1111/j.1365-246X.2008.03938.x)  
876 [j.1365-246X.2008.03938.x](http://doi.wiley.com/10.1111/j.1365-246X.2008.03938.x) doi: 10.1111/j.1365-246X.2008.03938.x
- 877 Savage, J. C., & Burford, R. O. (1973). Geodetic determination of relative plate  
878 motion in central California. *Journal of Geophysical Research*, *78*(5), 832–845.  
879 doi: 10.1029/JB078i005p00832
- 880 Scholz, C. H. (1998). Earthquakes and friction laws. *Nature*, *391*(6662), 37–42. doi:  
881 10.1038/34097
- 882 Socquet, A., Valdes, J. P., Jara, J., Cotton, F., Walpersdorf, A., Cotte, N., ... Nor-  
883 abuena, E. (2017). An 8 month slow slip event triggers progressive nucleation  
884 of the 2014 Chile megathrust. *Geophysical Research Letters*, *44*(9), 4046–4053.  
885 doi: 10.1002/2017GL073023
- 886 Steinbrugge, K. V., Zacher, E. G., Tocher, D., Whitten, C. A., & Claire, C. N.  
887 (1960). Creep on the San Andreas fault. *Bulletin of the Seismological Society*  
888 *of America*, *50*(3), 389–415.
- 889 Sudhaus, H., & Jónsson, S. (2009). Improved source modelling through combined  
890 use of InSAR and GPS under consideration of correlated data errors: appli-  
891 cation to the June 2000 Kleifarvatn earthquake, Iceland. *Geophysical Journal*  
892 *International*, *176*(2), 389–404. doi: 10.1111/j.1365-246X.2008.03989.x
- 893 Thomas, M. Y., Avouac, J.-P., Gratier, J.-P., & Lee, J.-C. (2014, June). Litho-  
894 logical control on the deformation mechanism and the mode of fault slip on  
895 the Longitudinal Valley Fault, Taiwan. *Tectonophysics*, *632*, 1–16. Re-  
896 trieved from <http://dx.doi.org/10.1016/j.tecto.2014.05.038> doi:  
897 10.1016/j.tecto.2014.05.038
- 898 Thomas, M. Y., Avouac, J.-P., & Lapusta, N. (2017). Rate-and-state friction proper-  
899 ties of the Longitudinal Valley Fault from kinematic and dynamic modeling of  
900 seismic and aseismic slip. *Journal of Geophysical Research-Solid Earth*, *122*(4),  
901 3115–3137. doi: 10.1002/2016JB013615

- 902 Wallace, L. M. (2020). Slow slip events in new zealand. *Annual Review of Earth*  
903 *and Planetary Sciences*, *48*(1), 175–203. doi: 10.1146/annurev-earth-071719  
904 -055104
- 905 Wei, M., Kaneko, Y., Liu, Y., & McGuire, J. J. (2013). Episodic fault creep events  
906 in California controlled by shallow frictional heterogeneity. *Nature Geoscience*,  
907 *6*, 566–570. doi: 10.1038/ngeo1835
- 908 Weiss, J. R., Walters, R. J., Morishita, Y., Wright, T. J., Lazecky, M., Wang, H.,  
909 ... Parsons, B. (2020, 11). High-resolution surface velocities and strain for  
910 anatolia from sentinel-1 insar and gnss data. *Geophysical Research Letters*,  
911 *47*(17), e2020GL087376. doi: 10.1029/2020GL087376
- 912 Williams, S. D. P. (2003). The effect of coloured noise on the uncertainties of rates  
913 estimated from geodetic time series. *Journal of Geodesy*, *76*(9-10), 483–494.  
914 doi: 10.1007/s00190-002-0283-4